Naval Research Laboratory
Washington, DC 20375-5000

NRL Memorandum Report 6844

Evolution of a Finite Pulse of Radiation in a High-Power Free-Electron Laser

A. TING, B. HAFIZI,* P. SPRANGLE AND C. M. TANG

Beam Physics Branch
Plasma Physics Division

**ICARUS Research*
Bethesda, Maryland 20814

June 20, 1991

REPORT DOCUMENTATION PAGE

Form Approved
OMB No 0704-0188

1. AGENCY USE ONLY (Leave blank)	2. REPORT DATE	3. REPORT TYPE AND DATES COVERED
	1991 June 20	Interim

4. TITLE AND SUBTITLE

Evolution of a Finite Pulse of Radiation in a High-Power Free-Electron Laser

5. FUNDING NUMBERS

ONR Contract
N00014-87-f-0066

JO#47-0899-0-1

6. AUTHOR(S)

A. Ting, B. Hafizi*, P. Sprangle and C. M. Tang

7. PERFORMING ORGANIZATION NAME(S) AND ADDRESS(ES)

NRL
Washington, DC 20375-5000

8. PERFORMING ORGANIZATION REPORT NUMBER

NRL Memorandum
Report 6844

9. SPONSORING/MONITORING AGENCY NAME(S) AND ADDRESS(ES)

ONR
Arlington, VA 22217

NIST
Gaithersburg, MD 20899

10. SPONSORING/MONITORING AGENCY REPORT NUMBER

11. SUPPLEMENTARY NOTES

*B. Hafizi, ICARUS Research, Bethesda, Maryland 20814

12a. DISTRIBUTION/AVAILABILITY STATEMENT

Approved for public release; distribution unlimited.

12b. DISTRIBUTION CODE

13. ABSTRACT *(Maximum 200 words)*

The development of an optical pulse of finite axial extent is studied by means of an axisymmetric, time-dependent, particle simulation code for different rates of tapering of the wiggler field. The results illustrate a number of the physical phenomena underlying the free-electron laser mechanism. These include: suppression of the sideband instability; the role of gain focusing versus that of refractive guiding; efficiency enhancement; and pulse slippage. It is found that a significant reduction in the sideband modulation of the optical field can be achieved with a faster tapering of the wiggler parameters. Increasing the tapering rate also reduces refractive guiding, causing the optical wavefronts to become more convex, thus spreading the optical field into a larger cross-section. The corresponding enhancement of the peak output power is associated with an increased lateral extent of the optical field rather than an increase in the field amplitude.

14. SUBJECT TERMS

Free-electron laser, sideband modulation, optical guiding, refractive guiding, gain focusing, efficiency enhancement

15. NUMBER OF PAGES

52

16. PRICE CODE

17. SECURITY CLASSIFICATION OF REPORT	18. SECURITY CLASSIFICATION OF THIS PAGE	19. SECURITY CLASSIFICATION OF ABSTRACT	20. LIMITATION OF ABSTRACT
UNCLASSIFIED	UNCLASSIFIED	UNCLASSIFIED	SAR

CONTENTS

EVOLUTION OF A FINITE PULSE OF RADIATION IN A HIGH-POWER FREE-ELECTRON LASER

I. Introduction

Many of the analyses and numerical studies of the free-electron laser (FEL) have been directed towards in-depth investigation of individual aspects of the underlying mechanism. What emerges is that the FEL interaction is sufficiently complex to be endowed with a variety of interesting physical phenomena.[1] The purpose of the present paper is to discuss the results from a numerical study in a sufficiently general setting wherein several of the phenomena of interest are simultaneously operative. The particular case examined is that of a high-current (~ kA), high-power (~ GW), short wavelength (~ μm), tapered-wiggler FEL. The results indicate that in addition to enhancing the extraction efficiency, tapering of the wiggler has the further benefit of improving the quality of the output by suppressing sideband modulation of the optical field. The role of optical guiding is emphasized. Specifically, the results are used to illustrate the characteristics associated with refractive guiding and gain focusing. The gradual transition between the two forms of guiding as the tapering rate is varied is discussed in detail.[2]

Manuscript approved April 4, 1991

II. Mathematical Model

The purpose of this section is to present the complete set of equations forming the basis of the numerical model. The vector potential of the optical field is given by

$$A_s = \frac{A}{2} \exp\left[i\left(\frac{\omega}{c} z - \omega t\right)\right] e_x + \text{c.c.},$$

where A is the slowly-varying envelope, ω is the radian frequency, c is the speed of light in vacuo, and e_x is the unit vector along the x axis. In the assumed azimuthally symmetric geometry considered, $a = |e|A/mc^2$ may be expanded as

$$a(r,z,t) = \sum_{n=0}^{\infty} a_n(z,t)\, L_n\left(2r^2/r_s^2\right) \times \exp\left[-(1 - i\alpha)\, r^2/r_s^2\right], \qquad (1)$$

where $-|e|$ is the charge on an electron of rest-mass m, L_n is the Laguerre polynomial of order n, and r is the radial coordinate. In this expansion $r_s(z,t)$ is the spot-size, $\alpha(z,t)$ is related to the curvature R^{-1} of the optical field by $R^{-1} = 2c\alpha/\omega r_s^2$, and $a_n(z,t)$, n = 0, 1, 2, ..., are the expansion coefficients. Substituting Eq. (1) into the well-known parabolic wave equation and employing the source-dependent expansion technique of Ref. 3, one obtains the following set of equations[4]

$$\left(\frac{\partial}{\partial t} + c\,\frac{\partial}{\partial z}\right) r_s = \frac{2c^2\alpha}{\omega r_s} - r_s c\, B_I, \qquad (2a)$$

$$\left(\frac{\partial}{\partial t} + c\,\frac{\partial}{\partial z}\right)\alpha = \frac{2c^2(1+\alpha^2)}{\omega r_s^2} + 2c\,(B_R - \alpha B_I), \qquad (2b)$$

$$\left(\frac{\partial}{\partial t} + c\,\frac{\partial}{\partial z} + c\,A_n\right) a_n = in\,Bc\,a_{n-1} + i(n+1)\,B^*\,ca_{n+1} - ic\,F_n, \qquad (2c)$$

where

$$F_n = \frac{-\nu}{N\omega c}\left(\frac{2c}{r_s}\right)^2 \sum_j \left(\frac{f_B a_w}{\gamma}\right)_j L_n\left(\frac{2r_j^2}{r_s^2}\right) \exp\left[-i\psi_j - (1+i\alpha)r_j^2/r_s^2\right], \quad (2d)$$

$$A_n = \frac{2ic}{\omega r_s^2}(2n + 1 - i\alpha) + i(2n\, B_R + B), \quad (2e)$$

$$B = F_1/a_o,$$

$$\equiv B_R + iB_I. \quad (2f)$$

In the formula for F_n, $\nu = I_b$ [kA]/17, where I_b is the electron beam current in kilo-Amperes, the summation is over the electrons at radial locations $\{r_j\}$ in a given ponderomotive bucket, N being the number of electrons initially therein; $\psi_j = (\omega/c + k_w)z_j - \omega t$ is the phase of the jth electron, located at z_j, relative to the ponderomotive wave. The normalized wiggler amplitude, a_w, is defined in Eq. (5d).

A detailed presentation of the source-dependent expansion approach is given in Ref. 3. For orientation, however, it should be noted that in vacuo one has the well-known result

$$r_s(z) = r_s(0)\left(1 + z^2/Z_R^2\right)^{1/2}, \quad (3a)$$

$$\alpha(z) = z/Z_R, \quad (3b)$$

where $r_s(0)$ is the minimum spot size (at $z = 0$) and

$$Z_R = \frac{\omega}{2c} r_s^2(0) \quad (3c)$$

is the Rayleigh range. These results follow from Eqs. (2) upon neglecting B, i.e., neglecting the electron beam, and assuming that the wavefronts are plane at z=0.

The scalar potential of the wiggler is represented by [5]

$$\chi = - (B_w/k_y) \cosh (k_x x) \sinh (k_y y) \cos (k_w z), \qquad (4)$$

where B_w is the induction and, for the parabolic pole faces considered herein, the wavenumbers along the three axes are related via $k_x = k_y = k_w/\sqrt{2}$. With the scalar potential given by Eq. (4), the betatron motion of the electrons is described by the quasi-classical (WKB) solutions

$$x_\beta = \frac{\hat{x}_\beta}{\sqrt{\omega_\beta}} \cos \left(\int^t dt' \, \omega_\beta(t') + \xi_x \right), \qquad (5a)$$

and

$$y_\beta = \frac{\hat{y}_\beta}{\sqrt{\omega_\beta}} \cos \left(\int^t dt' \, \omega_\beta(t') + \xi_y \right), \qquad (5b)$$

where $\hat{x}_\beta$, $\hat{y}_\beta$, ξ_x, and ξ_y are constants,

$$\omega_\beta = \frac{a_w c k_w}{2\gamma} \qquad (5c)$$

is the betatron frequency, and

$$a_w = \frac{|e| B_w}{k_w mc^2} \qquad (5d)$$

is the normalized wiggler amplitude.

Finally, the synchrotron motion of an electron of energy γmc^2 located at (z,r) is described by

$$\frac{d\gamma}{dt} = \frac{i\omega a_w f_B}{4\gamma} \sum_n a_n L_n \left(\frac{2r^2}{r_s^2} \right) \exp\left[i\psi - (1-i\alpha) r^2/r_s^2 \right] + \text{c.c.}, \qquad (6a)$$

$$\frac{d\psi}{dt} = ck_w - \frac{\omega}{2\gamma^2}\left[1 + \frac{1}{2}a_w^2 + \gamma^2\omega_\beta\left(\hat{x}_\beta^2 + \hat{y}_\beta^2\right)/c^2\right], \qquad (6b)$$

where $\psi = (\omega/c + k_w)\, z - \omega t$ is the phase of the electron in the ponderomotive wave, and $f_B = J_0(\zeta) - J_1(\zeta)$ is the usual[6] difference of Bessel functions with $\zeta = (a_w/2)^2/(1 + a_w^2/2)$.

III. Initialization

The initial electron distribution is as follows. The electrons are uniformly loaded on the mesh corresponding to the z axis, and they are weighted in such a way as to represent a parabolic density profile along z. For the transverse coordinates (x,v_x,y,v_y) the electrons are loaded randomly in such a way that i) the radial density profile is parabolic, and ii) the transverse velocity profile is Gaussian. The normalized edge emittance for such a distribution may be defined in a manner similar to that for a Gaussian-Gaussian distribution given in Ref. 7:

$$\varepsilon_x = 2\sqrt{6}\left[\langle x^2\rangle\langle\gamma^2\beta_x{}^2\rangle - \langle x\gamma\beta_x\rangle^2\right]^{1/2}, \tag{7}$$

and similarly for ε_y. Here $\langle\ldots\rangle$ indicates an average over the entire beam. For a monoenergetic electron beam with an initial parabolic radial density distribution

$$n_b(r) = n_o\,(1 - r^2/r_{bo}{}^2), \tag{8a}$$

and Gaussian velocity distribution

$$f(\beta_x,\beta_y) = \frac{1}{2\pi\sigma_x\sigma_y}\exp\left(-\frac{\beta_x{}^2}{2\sigma_x{}^2}\right)\exp\left(-\frac{\beta_y{}^2}{2\sigma_y{}^2}\right), \tag{8b}$$

the normalized edge emittance is given by

$$\varepsilon_{x,y} = 2\gamma r_{bo}\sigma_{x,y}, \tag{9}$$

where r_{bo} is the initial electron beam radius, σ_x and σ_y are the initial velocity space widths, and $\boldsymbol{\beta} = (v_x/c, v_y/c, v_z/c)$.

From Eq. (6b) the relativistic factor for a synchronous (i.e., resonant) electron with no betatron motion is given by $d\psi_r/dt = 0$:

$$\gamma_r^2 = \frac{1}{2}\,(\omega/ck_w)\,(1 + \tfrac{1}{2}a_w^2). \qquad (10)$$

The form of tapering employed in the computations is obtained simply by prescribing a constant rate of decrease of energy $d\gamma_r/dz < 0$ for a synchronous electron. With $d\gamma_r/dz$ equal to a given constant, one obtains $a_w(z)$ from Eq. (10).

The parameters for the computations presented herein are listed in Tables I and II. The high-current, high-energy electron beam would correspond to an rf linear accelerator similar to that at the Boeing Aerospace Company (BAC).[8] It must be pointed out that, to reduce run-time on the computer, the electron pulse length used here is shorter than that at BAC.

The initial intrinsic energy spread is taken to be zero. The last two terms in Eq. (6b), which are due to wiggler gradients, vary with the initial conditions for each electron, but are approximately constant along any individual orbit. This is, of course, the principal virtue of canted magnetic pole faces.[5] Hence, there is no constraint on the bucket height from wiggler gradients as such. However, there is an effective energy spread due to emittance which must, for a tapered wiggler, be less than the bucket height. From Eq. (6b) it is simple to show that the shift $\delta\gamma_r$ in the synchronous energy γ_r, defined by Eq. (10), due to the initial spread in transverse coordinates and velocities is given by

$$\left[\frac{\delta\gamma_r}{\gamma_r}\right]_{\text{emit}} = \frac{\left(\varepsilon_x^2 + \varepsilon_y^2\right)/2}{\left(2r_{bo}\right)^2\left(1 + a_w^2/2\right)}\,, \qquad (11)$$

where ε_x, ε_y and r_{bo} are defined by Eqs. (7) and (8a). To derive Eq. (11) use has been made of the fact that, for a matched electron beam, the electron beam envelope equation implies[9]

$$k_\beta \langle x^2 \rangle = \frac{\varepsilon_x}{2\sqrt{6}\gamma_r} , \tag{12}$$

and that, from (8a), $\langle x^2 \rangle = r_{bo}^2/6$. Here, $\langle x^2 \rangle$ indicates the average of x^2 taken with respect to the weight function given by the density $n_b(r)$, Eq. (8a). In Eq. (12) k_β, the betatron wave number, is related to the betatron frequency in Eq. (5c) via

$$\omega_\beta = \beta_z c k_\beta . \tag{13}$$

There is, of course, a condition identical to Eq. (12) relating $\langle y^2 \rangle$ to ε_y.

Retaining the lowest order optical mode a_o in Eq. (6a) and dropping the betatron terms in Eq. (6b), the full ponderomotive bucket height for electrons on axis is given by[10]

$$\left[\frac{\delta\gamma_r}{\gamma_r}\right]_{\text{bucket}} = \left\{ \frac{2a_w |a_o| f_B}{\left(1 + a_w^2/2\right)} \left[\cos \xi_r - \left(\frac{\pi}{2} \operatorname{sgn}\xi_r - \xi_r\right)\sin\xi_r\right] \right\}^{1/2} , \tag{14}$$

where

$$a_o = |a_o| \exp (i\phi), \tag{15}$$

$$\xi_r = \psi_r + \phi, \tag{16}$$

γ_r is defined by Eq. (10), and the phase ψ_r is related to the rate of change of γ_r in the tapered FEL by

$$\frac{d\gamma_r}{dt} = - \frac{a_w |a_o| \omega f_B}{2\gamma_r} \sin (\psi_r + \phi). \tag{17}$$

Table II lists the full bucket height for the various tapering rates $d\gamma_r/dz = c^{-1}\, d\gamma_r/dt$ employed in the computations. Comparing the set of bucket heights with the effective energy spread due to emittance,

$[\delta\gamma_r/\gamma_r]_{emit}$, one observes that for the input power of 450 MW essentially all the electrons are initially trapped. Also listed in Table II are the initial resonance phases ξ_r, Eq. (16), for the various tapering rates. Note that since in the computations $d\gamma_r/dz$ is prescribed to have a fixed value throughout a run, in general ξ_r is a variable through the wiggler.

IV. Results and Discussion

In this section numerical results from the solution of Eqs. (2), (5) and (6) are presented. As mentioned in the Introduction, the results will be used to illustrate some of the key physical phenomena of the FEL mechanism.[2] These include sideband growth,[10-18] optical guiding,[3,10,19-28] efficiency enhancement,[10,19,20] and pulse slippage.

As indicated in Table II the conclusions presented in this paper are based on numerical results that cover a wide range of tapering rates. For brevity, the results for only two tapering rates will be discussed. Case (a), $-d\gamma_r/dz = 0.1\ m^{-1}$ has a slow taper, and Case (b), $-d\gamma_r/dz = 1.3\ m^{-1}$ has a fast taper. The two cases discussed in detail suffice since there is a gradual change in the physical characteristics in going from one tapering rate to the next. The corresponding tapering of the wiggler amplitude, a_w, is shown in Figs. 1 (a) and (b), where a_w barely changes for Case (a). As shown in Figs. 2 (a) and (b), the resonant angle for Case (a) starts out to be $\xi_r = 2.6°$ and soon settles down to approximately $\xi_r \sim 1.5°$, while for Case (b) the resonant angle changes from an initial value of 36.5° to a final value of ~ 23°. In general, the resonance phase, $\xi_r \equiv \psi_r + \phi$, Eq. (16), varies along the wiggler. For all the tapering rates indicated in Table II, it is found that after an initial transient, ξ_r settles down to a fairly constant value through the rest of the run. The gain in radiation power along the wiggler is shown in Figs. 3 (a) and (b). The tapering rate in Case (b) is close to the optimal value and Fig. 3 (b) shows substantial increase in the output radiation power.

(a) Sideband Instability and Pulse Modulation

Ordinarily, tapering of the wiggler field is a means of enhancing the extraction efficiency of a FEL. In previous work it has been shown that tapering has the additional benefit of reducing sideband

modulation.[2,4,12,15] In particular, it is shown in Ref. 4 that as the tapering rate is increased, the modulation of the output signal due to sideband frequencies is reduced. Of course, there is an optimal rate of taper, beyond which excessive electron detrapping from the ponderomotive buckets leads to a reduction in the extraction efficiency.

For the finite pulse simulations, it also turns out that the tapering rate has a dramatic effect on the profile of the output optical pulse. This is illustrated rather well in Figs. 4 (a) and (b) which display the normalized radiation field amplitude a (z) at the wiggler exit, and Figs. 5 (a) and (b) which show the longitudinal profiles of the power in the radiation pulses for Cases (a) and (b). Figures 6 (a) and (b) show the transverse profiles of the radiation pulse for Cases (a) and (b). Note that in all the profiles for Case (a), there is significant amount of modulation. The respective spatial Fourier spectra $|a(\lambda)|$ as a function of wavelength λ are shown in Figs. 7 (a) and (b). The Fourier spectrum for the slow taper, Fig. 7(a), indicates two prominent sidebands on either side of the main component, the anti-Stokes sideband in the vicinity of 0.9775 μm and the Stokes sideband in the vicinity of 0.9915 μm. The two sidebands are seen to be of approximately equal amplitude and of equal separation relative to the carrier. For the fast taper, Fig. 7(b), we notice that the sidebands are significantly reduced compared to those in Fig. 7(a). It is interesting to note that the carrier components and the anti-Stokes components have merged into a broad-band feature in Fig. 7(b).

As is well-known, the wavelengths of the upper and the lower sidebands are given by [10-14]

$$\lambda_{sb} \simeq \frac{\lambda_s}{1 \pm \left(\frac{2a_w|a_o|f_B}{1 + a_w^2/2}\right)^{1/2}}, \qquad (18)$$

where $\lambda_s = 2\pi c/\omega$ is the wavelength of the carrier. The expression in (18) is based on the assumption that, in the trapped particle regime, electrons undergo synchrotron oscillations in the ponderomotive potential wells. From Fig. 7(a), the wavelength of the sideband radiation is within 10% of that given by Eq. (18). Coupling of a parasitic wavelength λ_{sb} to the carrier at λ_s via the synchrotron oscillations leads to a maximum growth of the instability when Eq. (18) is satisfied. In the presence of the sidebands, the optical field will be modulated at a wavelength λ_{mod} given by

$$\lambda_{mod} \simeq \left(\frac{1 + a_w^2/2}{2a_w|a_o|f_B}\right)^{1/2} \lambda_s. \qquad (19)$$

Taking $|a_o| \simeq 0.8\times10^{-4}$, the modulation period predicted by (19) has the approximate value 0.12 mm, which is in close agreement with the period of the prominent oscillations observed in Figs. 4(a) and 5(a). The close agreement is, however, fortuitous due to several reasons. For one thing, Eq. (19) is derived in a one-dimensional calculation for the case where $|a_o|$ is constant in z, whereas there is significant modulation (~ 100%) of the amplitude in Fig. 4(a). Additionally, for the finite pulse case examined here there is a spread in the wavelength of the main signal and this leads to the rather complicated spectral distribution observed in Fig. 7(a).

The asymmetric profile of the optical pulse in Figs. 4(b) and 5(b) may be understood in the following way. At the wiggler entrance, the electron

pulse and the optical pulse are symmetric in z and superimposed on top of each other. Along the wiggler, the electron pulse slips behind relative to the optical pulse, thus tending to amplify the trailing side of the latter more than the leading edge. Still farther behind along the trailing side of the optical pulse, the field amplitude is so small that a substantial fraction of electrons are not trapped in the ponderomotive bucket. This, in conjunction with the fact that diffraction further reduces the field amplitude for $0 \leq z \leq 1$ mm, accounts for the very small amplitude in this region.

In Fig. 8 (a) and (b) the extraction efficiency is shown for the two tapering rates, Cases (a) and (b). As usual, the efficiency, for the slower tapering rate, is modulated by the synchrotron oscillations of the electrons. For the more rapid rate of tapering the synchrotron oscillations are barely noticeable. Note also that there is a ten-fold improvement in the efficiency compared to the slower tapering rate.

Tapering reduces sideband modulation by decreasing the trapping fraction and by distorting the synchrotron motion.[4,12] The trapping fraction drops from ~ 40% in Case (a) to ~ 35% in Case (b). A measure of the distortion of electron orbits is given by[4]

$$Q \equiv \left| \frac{c(d\gamma_r/dz)}{\langle \Omega_{syn}(\gamma-\gamma_r)\rangle} \right| \tag{20}$$

where

$$\Omega_{syn} = ck_w \left[\frac{2a_w|a_o|f_B}{1 + a_w^2/2}\right]^{1/2} \tag{21}$$

is the synchrotron frequency. Q is the ratio of the change in energy $cd\gamma_r/dz$ due to tapering and the change in energy $\langle\Omega(\gamma - \gamma_r)\rangle$ due to

synchrotron motion. For Case (a), Q ≈ 1%, indicating a slight distortion, whereas for Case (b), Q ≈ 25%, indicating significant modification of the synchrotron motion and thus, reduced sideband modulation as is indeed observed in Fig. 4(b) and 5(b).

(b) Optical Guiding

Optical guiding in the context of FELs has been the subject of numerous discussions.[1] Briefly, the resonant interaction between the electrons and the optical field tends to guide the radiation along the direction of the electron beam.

Two causes of guiding,[3,10,19-25] gain focusing and refractive guiding, have been distinguished based on the notion of a complex refractive index.[24] In general these two participate simultaneously and their combined effect on the spot size can only be ascertained via the envelope equation for the radiation beam in an FEL.[3] Refractive guiding, which is described by the reactive (real) part of the refractive index, is due to the phase shift of light, as implied by the fact that $v_{phase} < c$.[10,20,21] A distinguishing characteristic of this type of guiding is that the optical wavefronts are plane under the conditions of perfect guiding. The other type of guiding, gain focusing, is described by the resistive (imaginary) part of the refractive index. In this case, under the conditions of perfect guiding, the wavefronts are convex, corresponding to the fact that there is a net power flow, due to diffraction, away from the electron beam.

Figures 9 (a) and (b) show the spot size $r_s(z)$ (dashed line), and wave-front curvature $R^{-1}(z)$ (solid line) for Cases (a) and (b). In Fig. 9 (a), which correspond to the slow taper, one discerns the modulations characteristic of sidebands, as in Figs. 4 (a) and 5 (a). Besides the modulations, however, Fig. 9 shows a dramatic example of optical guiding. Referring to Figs. 4 (a) and (b), it is apparent that in the region where

the optical field amplitude is significant, the spot size of the radiation is considerably smaller than in neighboring regions. In fact, in Fig. 9 in the regions $z \leq 1.0$ mm or $z \geq 3.0$ mm the spot size r_s and curvature R^{-1} take on values corresponding to vacuum diffraction from the initial values of r_s and R^{-1} at the wiggler entrance. This is obviously as it should be, since there is hardly any radiation in these two regions ($z \leq 1.0$ mm and $z \geq 3.0$ mm) during the simulation.

Another significant feature of Fig. 9 is revealed by noting that the curvature of the wavefronts R^{-1} is less for the less rapidly tapered case. In particular, in the vicinity of $z \simeq 1.2$ mm in Fig. 9(a), the curvature is negative, indicating that the wavefronts in this region are in fact concave. On the other hand, in the case of rapid tapering, Fig. 9(b), the wavefronts are convex all through the pulse, indicating a flow of power away from electron beam throughout the pulse.

To shed more light on this behavior, it is useful to compare the refractive index of the FEL for these two cases. Using a refractive index $\mu(r,z,t)$ to represent the entire FEL interaction, the vector potential may be written as[3,10,20,21,27]

$$a(r,z,t) \sim e^{i\Phi} \tag{22a}$$

$$\Phi = \frac{\omega}{c} z - \frac{\omega}{\mu} t, \tag{22b}$$

where

$$\mu = 1 + (\omega_b/\omega)^2 (a_w/2|a|) \langle \exp(-i\xi)/\gamma \rangle, \tag{22c}$$

ω_b is the electron beam plasma frequency and $\langle \cdots \rangle$ denotes an average over the local particle distribution. In terms of F_n defined by Eq. (2d),

$$\mu\,(r,z,t) = 1 - \frac{1}{2}\,\frac{c}{\omega}\,\frac{\sum_{n=0}^{\infty} F_n L_n\left(2r^2/r_s^{\,2}\right)}{\sum_{n=0}^{\infty} a_n L_n\left(2r^2/r_s^{\,2}\right)}\,.$$

Figures 10 (a) and (b) show the real part (Real(μ) - 1) and Figs. 11 (a) and (b) show the imaginary part (Imag.(μ)) of the refractive index on axis, r = 0, at the end of the wiggler for Cases (a) and (b). Comparing Figs. 10 (a) and (b) it is apparent that there is more refractive guiding in the former case, which is the less rapidly tapered example. This is consistent with the fact that for slow tapering, $\xi_r \ll 1$,

$$\mathrm{Re}\mu - 1 \sim \left\langle \frac{\cos \xi_r}{\gamma} \right\rangle, \tag{23a}$$

dominates over the gain term

$$\mathrm{Im}\mu \sim - \left\langle \frac{\sin \xi_r}{\gamma} \right\rangle. \tag{23b}$$

Equation (23) is obtained by making use of Eqs. (2d), (15) and (16). On the other hand, the more rapidly tapered case of Fig. 11 (b) is seen to have a larger net gain in the region where the optical field is significant. [Note from Eqs. (22) that Imμ < 0 corresponds to gain.] In the same region, Fig. 11 (a) indicates that the net gain is approximately zero after averaging over the synchrotron modulations. Again, this feature of Figs. 11 (a) and (b) is consistent with the fact that in the latter the tapering rate is faster and therefore the gain should be larger. Moreover, it is seen in Figs. 9 (a) and (b) that the larger gain corresponds to a more convex optical wavefront.

The implication of these results with regard to the spot size may be ascertained by a consideration of the terms in K^2 in the envelope equation[3]

$$r_s'' + K^2(z,t,r_s,|a_0|)r_s = 0,$$

$$K^2 \equiv (2c/\omega)^2(-1 + 2C\cos\xi_r + C^2\sin^2\xi_r + (\omega/2c)r_s^2C'\sin\xi_r)r_s^{-4},$$

where a_0 is the amplitude of the fundamental Gaussian mode, $C=(2I_b/17\gamma_r)Ha_w/|a_0|$, $' \equiv \partial/\partial z + c^{-1}\partial/\partial t$, I_b is the beam current in kilo-Amperes, H, which is a form-factor related to the transverse profile of the electron beam, is roughly a constant and close to unity herein, γ_r is the relativistic factor for a resonant electron, and ξ_r is the resonance phase approximation for $\langle\xi\rangle$. The -1 in the expression for K^2 is due to vacuum diffraction, $2C\cos\xi_r$ contributes to refractive guiding arising from the real part of μ, the third and the fourth terms, due to the imaginary part of μ, contribute to gain focusing. Taking account of the fraction of trapped electrons, one finds that in going from Case (a) to Case (b) the gain-focusing term $C^2\sin^2\xi_r$ increases from 2.4×10^{-3} to 7×10^{-2}. The other term, $(\omega/2c)r_s^2C'\sin\xi_r$, changes from -4.4×10^{-3} to -2.4×10^{-2}, the negative sign indicating a defocusing contribution. On the other hand, the refractive guiding term $2C\cos\xi_r$ decreases from 3.1 to 1.6. The increase in the magnitude of the gain focusing terms in going from Case (a) to Case (b) is principally due to the increase in ξ_r. Concurrently, the 50% reduction in the refractive guiding term is due to the increase in $|a_0|$ and the decrease in a_w. Since the refractive guiding term is the dominant term, the reduction in its value leads to a decrease in K^2, and hence to reduced optical guiding. The net effect is the increase in the spot size and the curvature observed in Fig. 9(b) as compared to Fig. 9(a). In other words, the wavefronts become increasingly convex with faster tapering rate.

It should be remarked that since the peak output field amplitudes for the two different tapering rates are about equal [cf. Figs. 4 (a) and (b)],

the increased peak output power of the more rapidly tapered case is principally due to the larger spot size. Thus, by increasing the tapering rate there results a reduction in the refractive guiding; however, the increased gain then causes the wavefronts to become more convex, diffracting the optical field into a larger cross-section. As a result the output power, which is proportional to $(|a|r_s)^2$, increases as shown in Fig. 3(b). Detailed examination of the results for all the tapering rates indicates that the optical field amplitude is very little affected by tapering - aside from reducing synchrotron modulations. As a result, increased output power and extraction efficiency is principally due to the larger lateral extent of the optical field. This is in sharp contrast to the situation in one dimension wherein r_s is necessarily constant and increased efficiency can only come about as a result of an increase in the field amplitude.

Figure 12 summarizes the results for the nine tapering rates $-d\gamma_r/dz$ = 0.1, 0.3, ..., 1.7 m^{-1}, corresponding to final resonant angles $\xi_r \approx 1.8°$, 3.5°, ..., 35°. Beyond $-d\gamma_r/dz \approx 0.3\ m^{-1}$, the amplitude $|a|$ is fairly constant up to $-d\gamma_r/dz \approx 1.3\ m^{-1}$, after which it decreases. However, there is a near-monotonic increase in the spot size. Therefore, it is the increased transverse extent of the optical field -- and not an increase in intensity -- that is responsible for the enhancement in the power ($\propto |r_s a|^2$) observed in Figs. 3 (b) and 5 (b). Based on the desired output power and the constraint on the maximum spot size one can determine the optimal tapering from Fig. 12.

V. Conclusions

This paper presents the results from the simulation of a high-power, high-current, short wavelength FEL. The simulations include many of the important aspects of a realistic experiment, including finite-pulse effects, diffraction and emittance. A wide range of wiggler-field tapering rates have been examined. Summarizing the results, it is found that in addition to enhancing the efficiency, tapering improves the quality of the output by suppressing sideband growth. Further, it is found that as the tapering rate is increased there is a gradual transition from a refractive-guiding regime to one where gain focussing dominates, with optical power diffracting laterally along the convex wavefronts. The increased transverse extent of the optical field, rather than an increase in the field amplitude is the major reason for efficiency enhancement as the tapering rate is increased.

Acknowledgements

The authors are grateful to Drs. T. F. Godlove, I. Haber, W. P. Marable and C. W. Roberson for valuable suggestions. This work was supported by ONR through the National Institute of Standards and Technology.

References

1. C. W. Roberson and P. Sprangle, "A Review of Free-Electron Lasers", Phys. Fluids B, vol. 1, pp. 3-42 (1989).
2. B. Hafizi, A. Ting, P. Sprangle and C. M. Tang, "Efficiency Enhancement and Optical Guiding in a Tapered High-Power Finite-Pulse Free-Electron Laser", Phys. Rev. Lett., vol 64, pp. 180-183 (1990).
3. P. Sprangle, A. Ting and C. M. Tang, "Radiation Focusing and Guiding with Application to the Free-Electron Laser", Phys. Rev. Lett., vol. 59, pp. 202-205 (1987); "Analysis of Radiation Focusing and Steering in the Free-Electron Laser by Use of a Source-Dependent Expansion Technique", Phys. Rev. A, vol. 36, pp. 2773-2781 (1987).
4. B. Hafizi, A. Ting, P. Sprangle and C. M. Tang, "Development of Sidebands in Tapered and Untapered Free-Electron Lasers", Phys. Rev. A, vol. 38, pp. 197-203 (1988).
5. E. T. Scharlemann, "Wiggle Plane Focusing in Linear Wigglers", J. Appl. Phys., vol. 58, pp. 2154-2161 (1985).
6. A. A. Kolomenskii and A. N. Lebedev, "Stimulated Undulator Radiation from Relativistic Electrons and the Physical Processes in an 'Electron Laser'", Sov. J. Quantum Electron., vol. 8, pp. 879-884 (1978); W. B. Colson, "The Nonlinear Wave Equation for Higher Harmonics in Free-Electron Lasers", IEEE J. Quantum Electronics, vol. QE-17, pp. 1417-1427 (1981).
7. S. Penner, "RF Linac based Free Electron Lasers", in Proceedings of the 1987 IEEE Particle Accelerator Conference, March 1987, Washington, DC, edited by E. R. Lindstrom and L. S. Taylor (IEEE, New York, 1987), pp. 183-188.

8. T. F. Godlove and P. Sprangle, "High-Power free-Electron Lasers Driven by RF Linear Accelerators", Particle Accelerators, vol. 34, pp. 169-187 (1990); T. W. Meyer, R. L. Gullickson, B. J. Pierce and D. R. Ponikvar, "The Ground Based Free Electron Laser: Challenges and Solutions", Nucl. Instr. Meth. Phys. Res. A, vol. 285, pp. 369-373 (1989).

9. E. P. Lee and R. K. Cooper, "General Envelope Equation for Cylindrically Symmetric Charged-Particle Beams", Part. Accel., vol. 7, pp. 83-95 (1976).

10. N. M. Kroll, P. L. Morton and M. N. Rosenblutn, "Free-Electron Lasers with Variable Parameter Wigglers", IEEE J. Quantum Electron., vol. QE-17, pp. 1436-1468 (1981).

11. J. C. Goldstein and W. B. Colson, "Control of Optical Pulse Modulation due to the Sideband Instability in Free Electron Lasers", in Proceedings of the International Conference on Lasers, New Orleans, LA, 1982, edited by R. C. Powell (STS, McLean, VA, 1983), pp. 216-225; J. C. Goldstein, B. E. Newnam, R. W. Warren and R. L. Sheffield, "Comparison of the Results of Theoretical Calculations with Experimental Measurements from the Los Alamos Free Electron Laser Oscillator Experiment", Nucl. Instr. Meth. Phys. Res. A, vol. 250, pp. 4-11 (1986).

12. W. B. Colson, "The Trapped-Particle Instability in Free Electron Laser Oscillators and Amplifiers", Nucl. Instr. Meth. Phys. Res. A, vol. 250, pp. 168-175 (1986).

13. R. C. Davidson and J. S. Wurtele, "Single-Particle Analysis of the Free-Electron Laser Sideband Instability for Primary Electromagnetic Wave with Constant Phase and Slowly Varying Phase", Phys. Fluids, vol. 30, pp. 557-569 (1987).

14. S. Riyopoulos and C. M. Tang, "The Structure of the Sideband Spectrum in Free Electron Lasers", Phys. Fluids, vol. 31, pp. 1708-1719 (1988).

15. S. Y. Cai, A. Bhattacharjee, S. P. Chang, J. W. Dodd and T. C. Marshall, "Effects of Optical Guiding on Sideband Instabilities in a Free-Electron Laser", Phys. Rev. A, vol. 40, pp. 3127-3135 (1989).

16. J. N. Elgin, "Analysis of the Sideband Instability in the Free Electron Laser", Phys. Rev. A, vol. 43, pp. 2514-2523 (1991).

17. B. A. Richman, J. M. J. Madey and E. Szarmes, "First Observation of Spiking Behavior in the Time Domain in a Free-Electron Laser", Phys. Rev. Lett., vol. 63, pp. 1682-1684 (1939).

18. Y. Kishimoto, H. Oda and M. Shiho, "Parasitic Wave Excitation by Multimode Coupling in a Raman-Regime Free-Electron Laser", Phys. Rev. Lett., vol. 65, pp. 851-854 (1990).

19. P. Sprangle, C. M. Tang, and W. M. Manheimer, "Nonlinear Formulation and Efficiency Enhancement of Free-Electron Lasers", Phys. Rev. Lett., vol 43, pp. 1932-1936 (1979); "Nonlinear Theory of Free-Electron Lasers and Efficiency Enhancement", Phys. Rev. A, vol. 21, pp. 302-318 (1980).

20. D. Prosnitz, A. Szoke, and V. R. Neil, "High-Gain, Free-Electron Laser Amplifiers: Design Considerations and Simulation", Phys. Rev. A, vol. 24, pp. 1436-1451 (1981).

21. P. Sprangle and C. M. Tang, "Three-Dimensional Nonlinear Theory of the Free Electron Laser", Appl. Phys. Lett., vol. 39, pp. 677-679 (1981).

22. J. M. Slater and D. D. Lowenthal, "Diffraction Effects in Free-Electron Lasers", J. Appl. Phys., vol. 52, pp. 44-47 (1981).

23. G. T. Moore, "High-Gain Small-Signal Modes of the Free-Electron Laser", Optics Commun., vol. 52, pp. 46-51 (1984).

24. E. T. Scharlemann, A. M. Sessler, and J. S. Wurtele, "Optical Guiding in a Free Electron Laser", Nucl. Instr. Methods Phys. Res. A, vol. 239, pp. 29-35 (1985); "Optical guiding in Free-Electron Laser", Phys. Rev. Lett., vol. 54, pp. 1925-1928 (1985).

25. M. Xie and D. A. G. Deacon, "Theoretical Study of FEL Active Guiding in the Small Signal Regime", Nucl. Instr. Methods Phys. Res. A, vol. 250, pp. 426-431 (1986).

26. R. A. Jong, E. T. Scharlemann, and W. M. Fawley, "Wiggler Taper Optimization for Free Electron Laser Amplifiers with Moderate Space-Charge Effects", Nucl. Instr. Methods Phys. Res. A, vol. 272, pp. 99-105 (1988); J. E. La Sala, D. A. G. Deacon, and J. M. J. Madey, "Optical Guiding Measurements on the Mark III Free Electron Laser Oscillator", Nucl. Instr. Methods Phys. Res. A, vol. 272, pp. 141-146 (1988).

27. B. Hafizi, P. Sprangle and A. Ting, "Optical Gain, Phase Shift, and Profile in Free-Electron Lasers", Phys. Rev. A, vol. 36, pp. 1739-1746 (1987).

28. Y. Seo, V.K. Tripathi and C.S. Liu, "Radiation Guiding in a Free Electron Laser", Phys. Fluids B, vol. 1, pp. 221-229 (1989).

Table I. Parameters for a high-power, rf-linac FEL

Electron Beam	
Energy, γmc^2	175 MeV
Current, I_b	250 A
Normalized edge emittance, $\varepsilon_x = \varepsilon_y$	153 mm-mrad
Radius, r_{bo}	1 mm
Betatron period, $2\pi/k_\beta$	11.5 m
Pulse length	6.7 ps
Wiggler	
Induction, B_w	6.4 kG
Period, $2\pi/k_w$	4.7 cm
Length	42 m
Input Radiation	
Wavelength, $2\pi c/\omega$	1 μm
Spot size, $r_s(0)$	1.25 mm
Rayleigh range, Z_R	4 m
Radius of curvature of optical wavefronts, $Z_R/\alpha(0)$	10 m
Pulse length (FWHM)	31.4 ps
Peak input power	450 MW

Table II. Resonance phases and tapering rates (The energy spread due to emittance is approximately the same for all tapering rates)

$d\gamma_r/dz$ (m^{-1})	Initial Resonance Phase ξ_r (°)	Full bucket height $[\delta\gamma_r/\gamma_r]_{bucket}$ (%)	Energy spread due to emittance $[\delta\gamma_r/\gamma_r]_{emit}$ (%)
-0.1	2.6	0.96	
-0.3	7.9	0.89	
-0.5	13.2	0.82	
-0.7	18.7	0.75	
-0.9	24.3	0.68	0.12
-1.1	30.2	0.6	
-1.3	36.5	0.5	
-1.5	41.2	0.44	
-1.7	48.0	0.35	

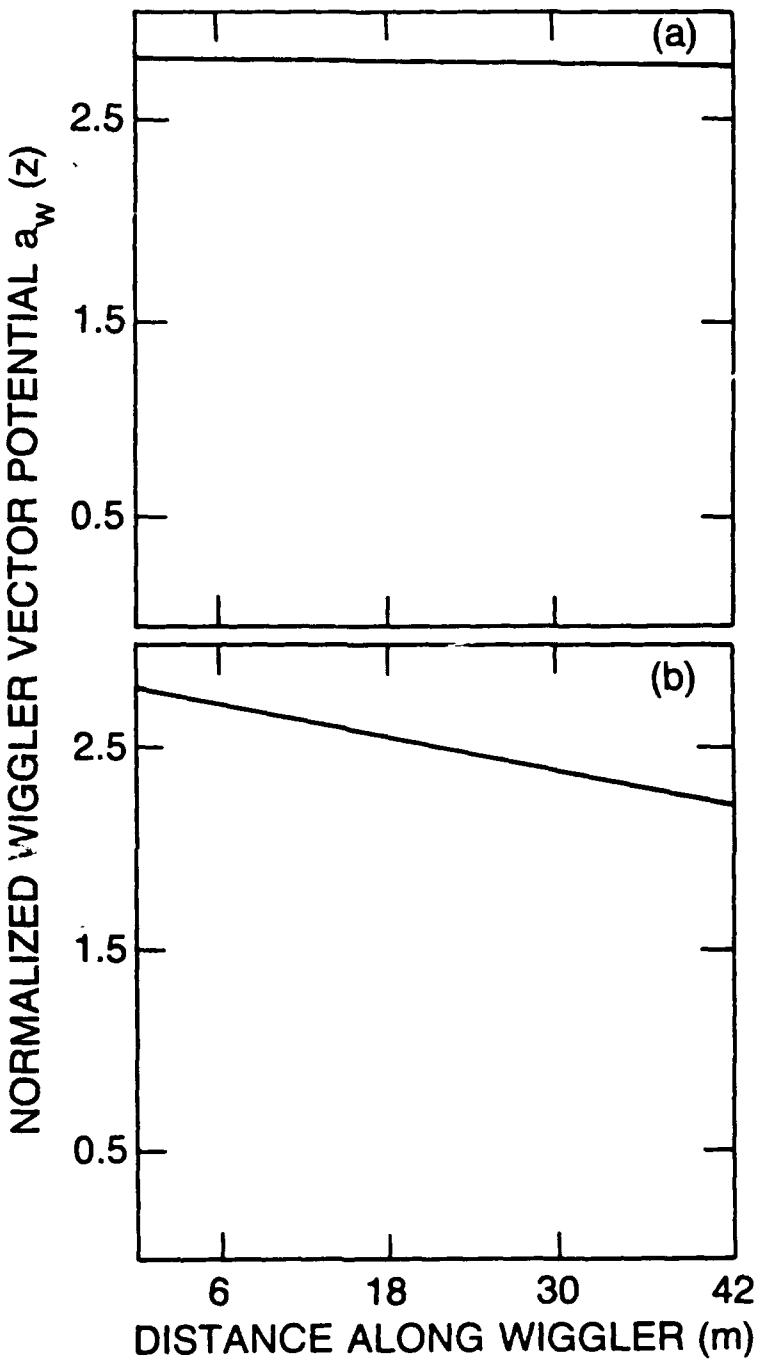

Fig. 1 Tapering of normalized wiggler amplitude along the wiggler. Radiation Power in GW at wiggler exit. (a) slow tapering rate, $d\gamma_r/dz = -0.1\ m^{-1}$, Case (a); (b) rapid tapering rate, $d\gamma_r/dz = -1.3\ m^{-1}$, Case (b).

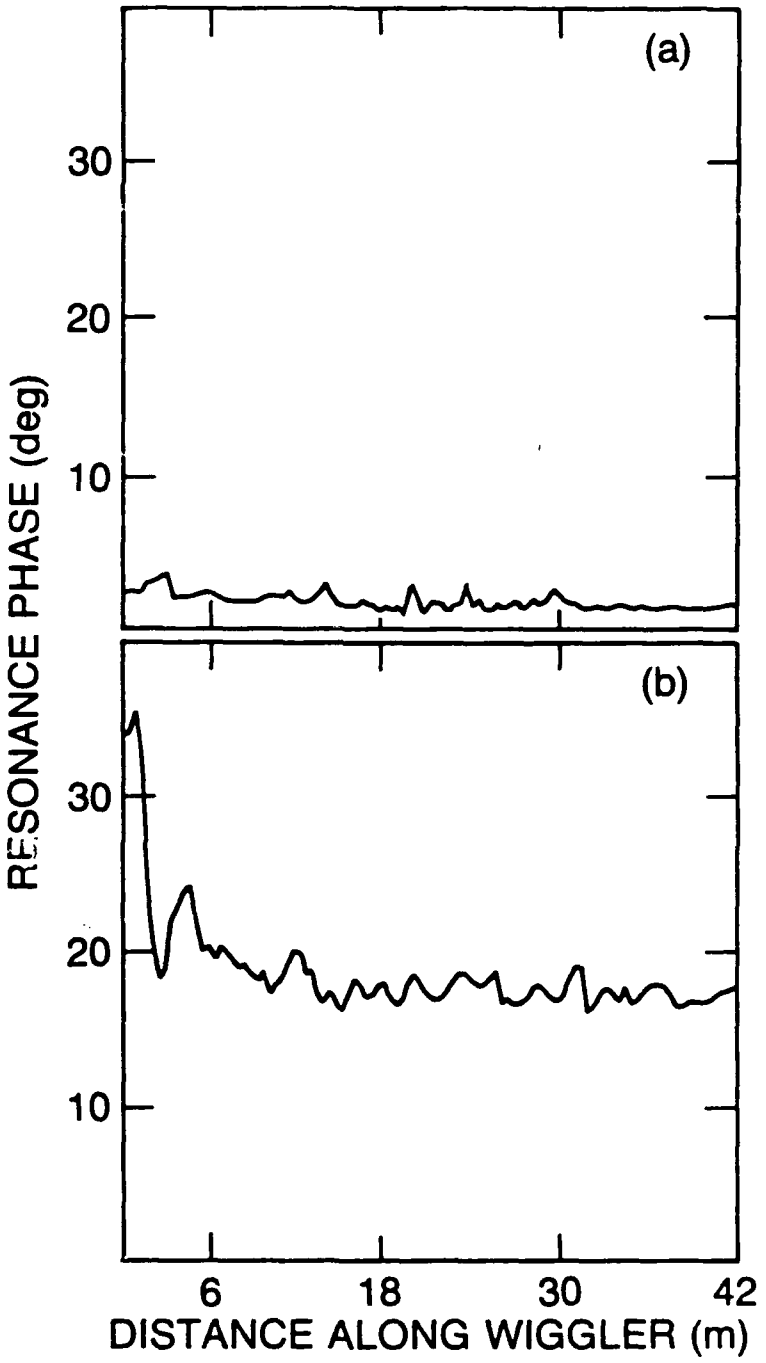

Fig. 2 Resonance phase ξ_r versus distance along the wiggler. (a) slow taper, Case (a); (b) rapid taper, Case (b).

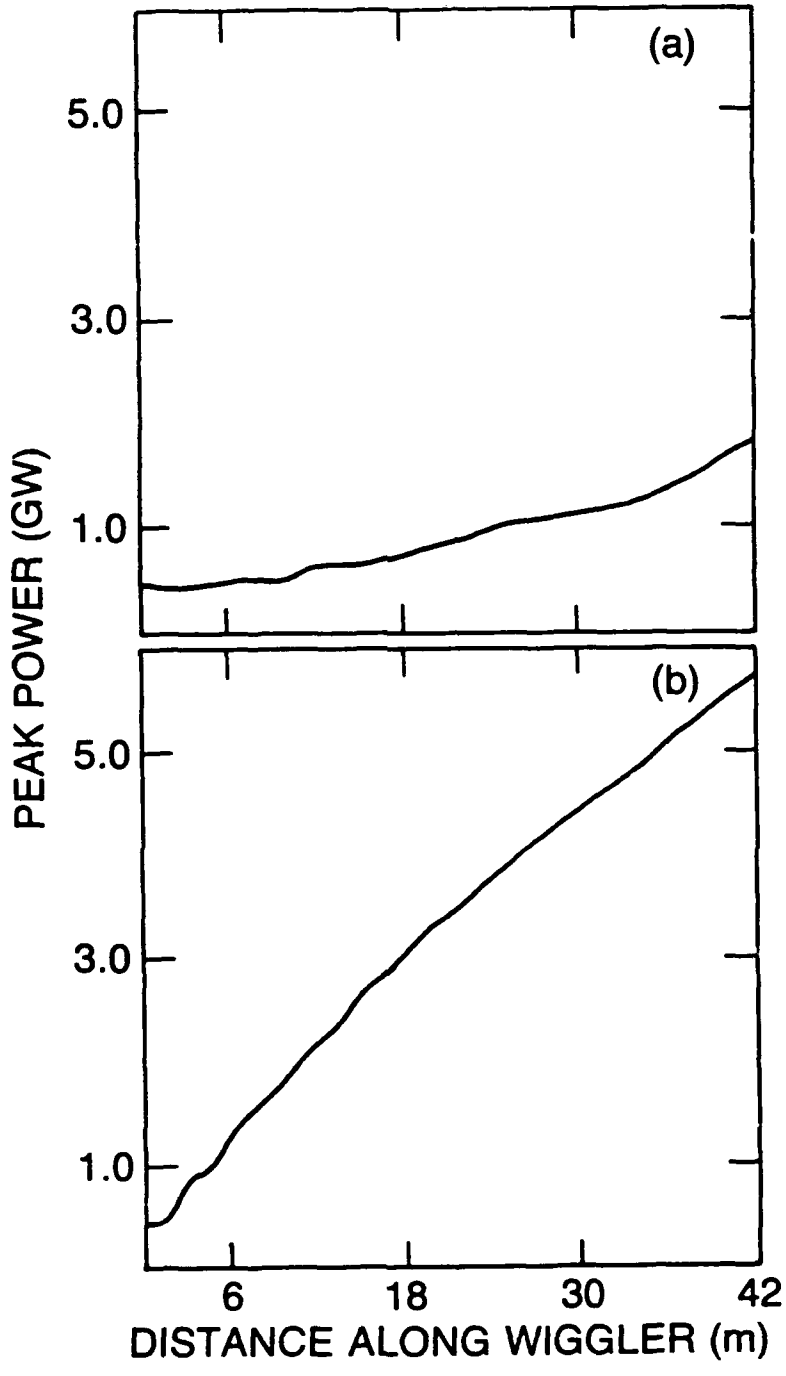

Fig. 3 Increase in peak power along the wiggler. (a) slow taper, Case (a); (b) rapid taper, Case (b).

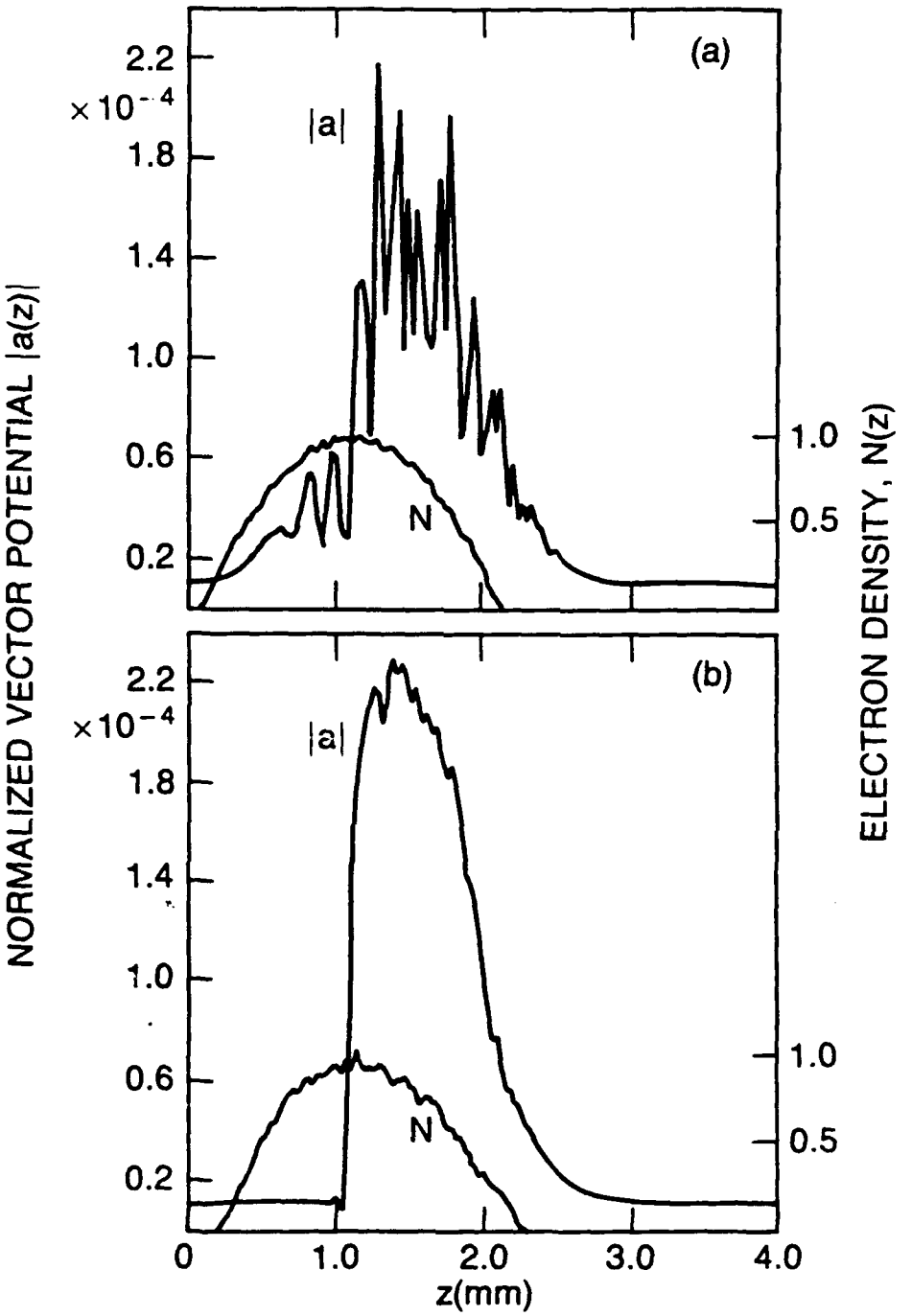

Fig. 4 Vector potential $|a(z,r=0)|$ and linear electron density N(z) at wiggler exit. (a) slow taper, Case (a); (b) rapid taper, Case (b). Note that intensity $\propto |a|^2$.

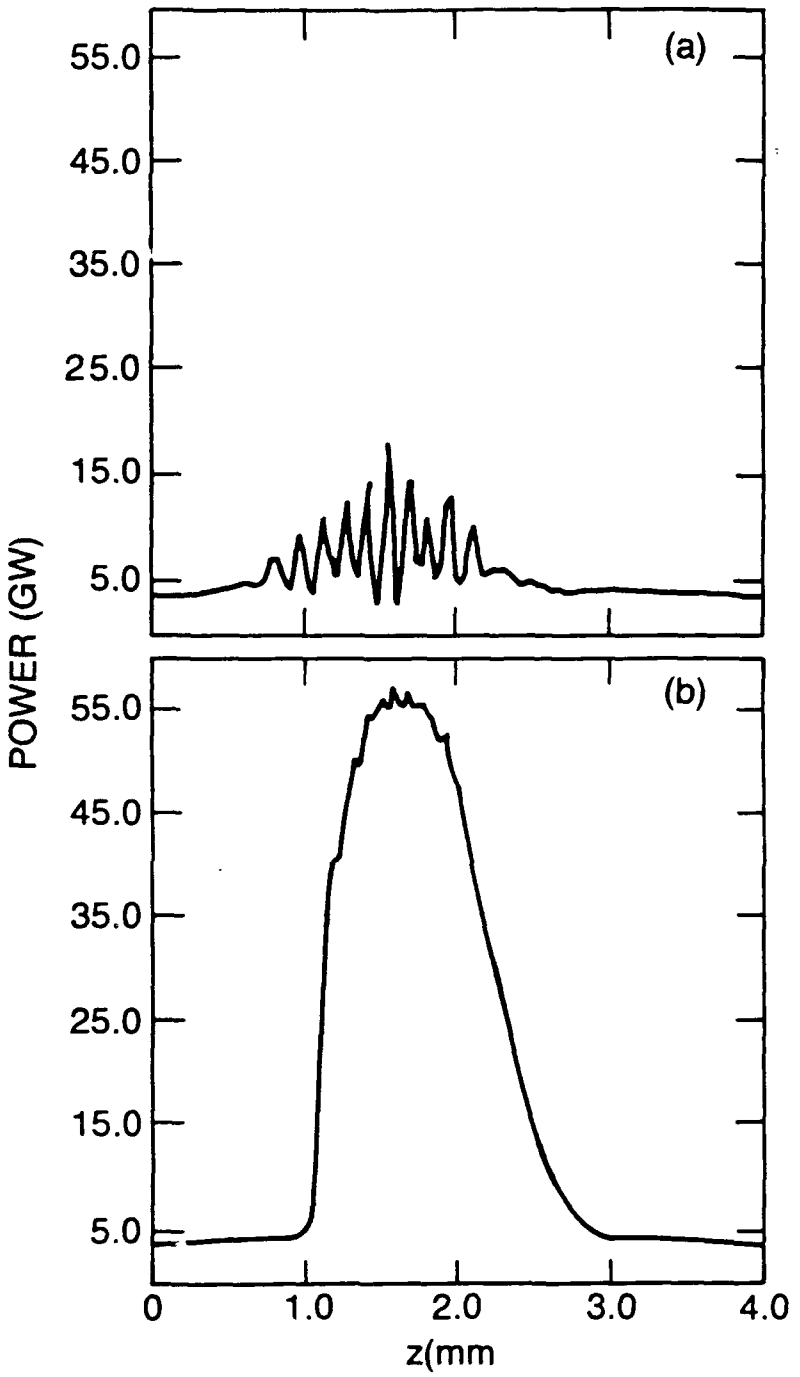

Fig. 5 Radiation Power in GW at wiggler exit. (a) slow taper, Case (a); (b) rapid taper, Case (b).

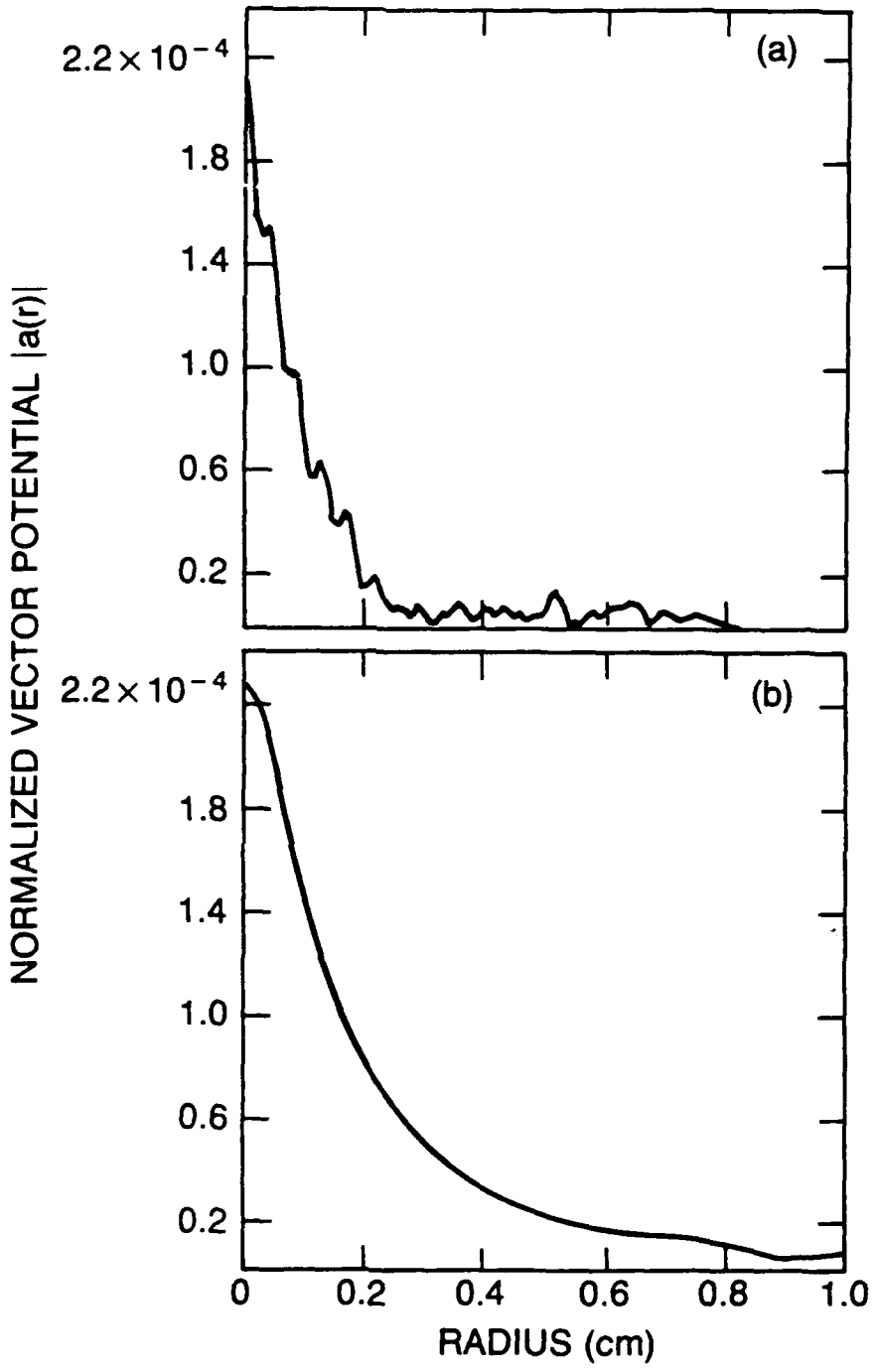

Fig. 6 Radial profile of normalized vector potential $|a(r)|$ at wiggler exit. (a) slow taper, Case (a); (b) rapid taper, Case (b).

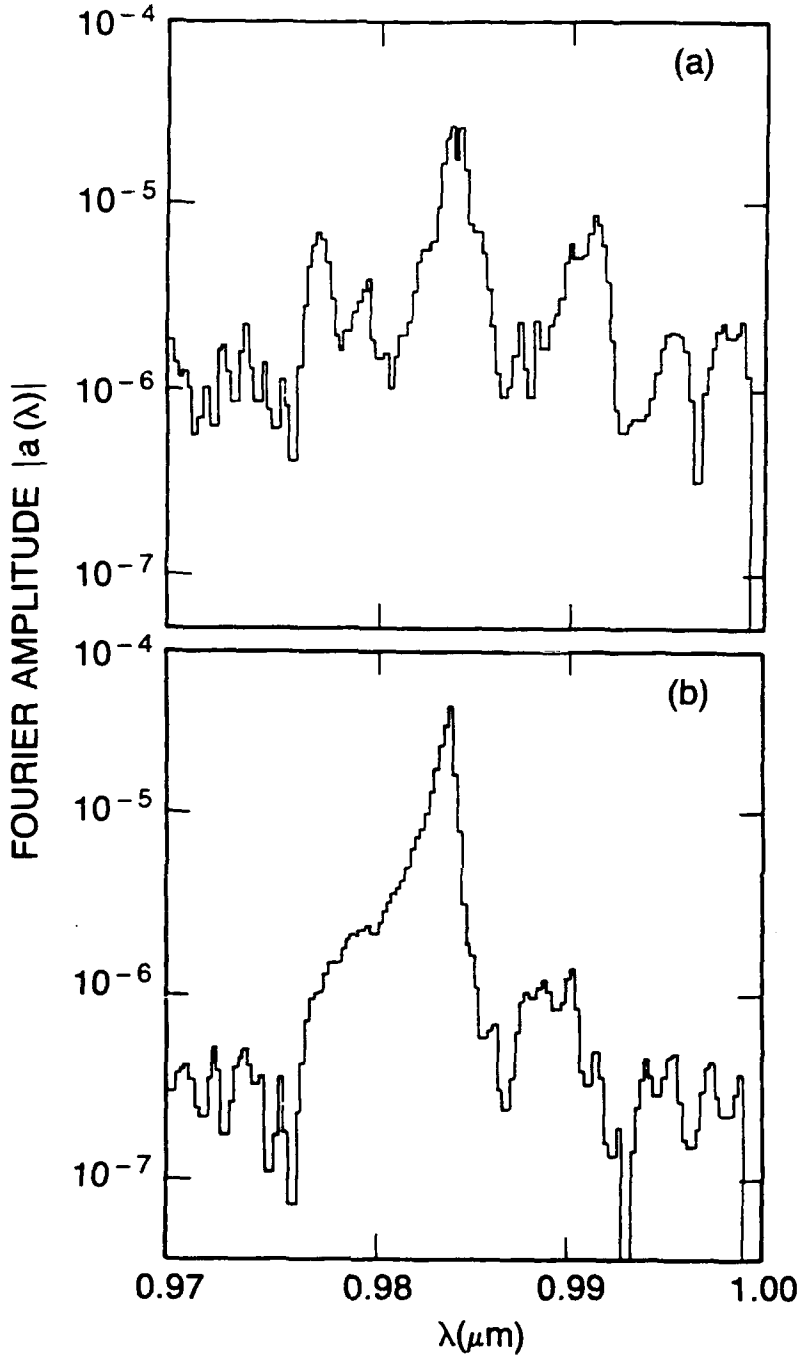

Fig. 7 Fourier spectrum of radiation amplitude $|a(\lambda)|$ at wiggler exit. (a) slow taper, Case (a); (b) rapid taper, Case (b).

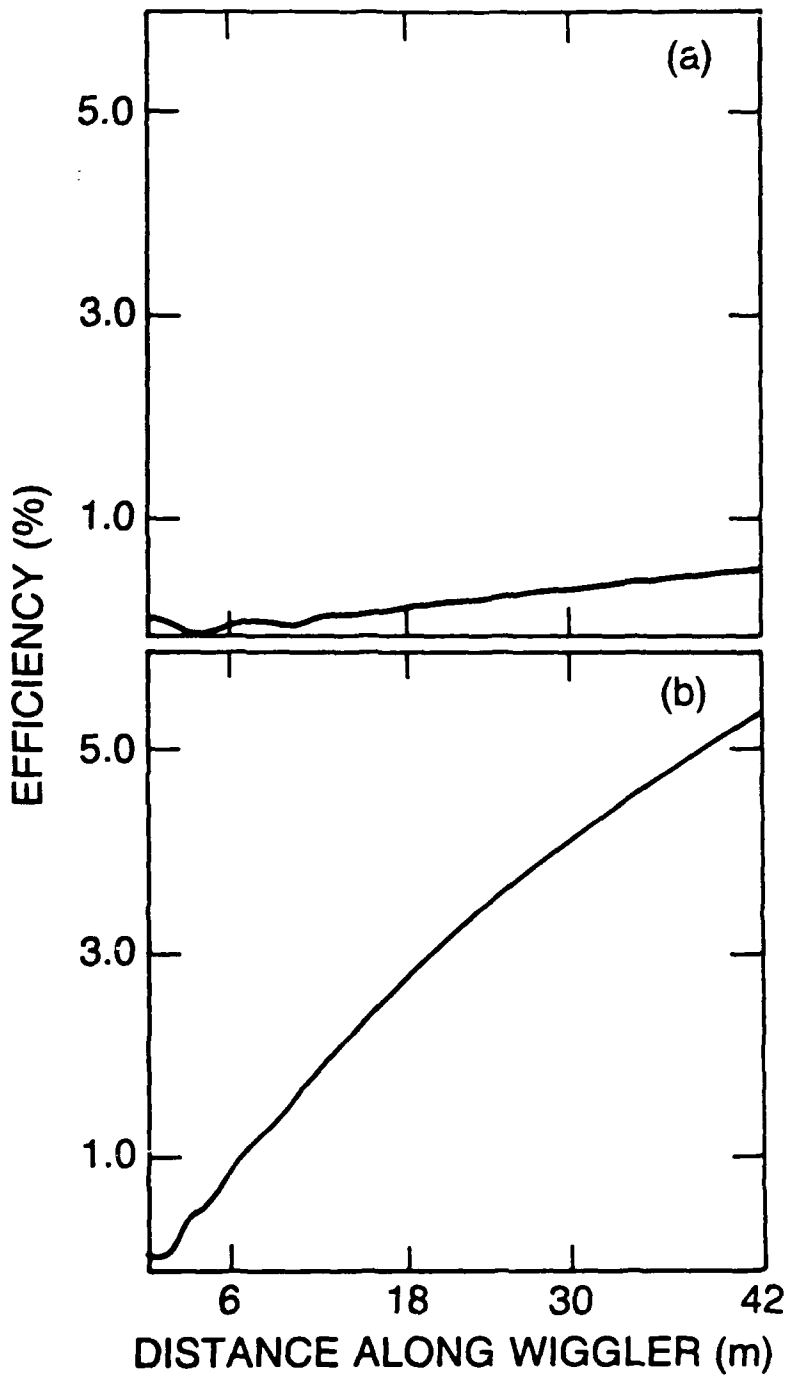

Fig. 8 Extraction efficiency along the wiggler. (a) slow taper, Case (a); (b) rapid taper, Case (b).

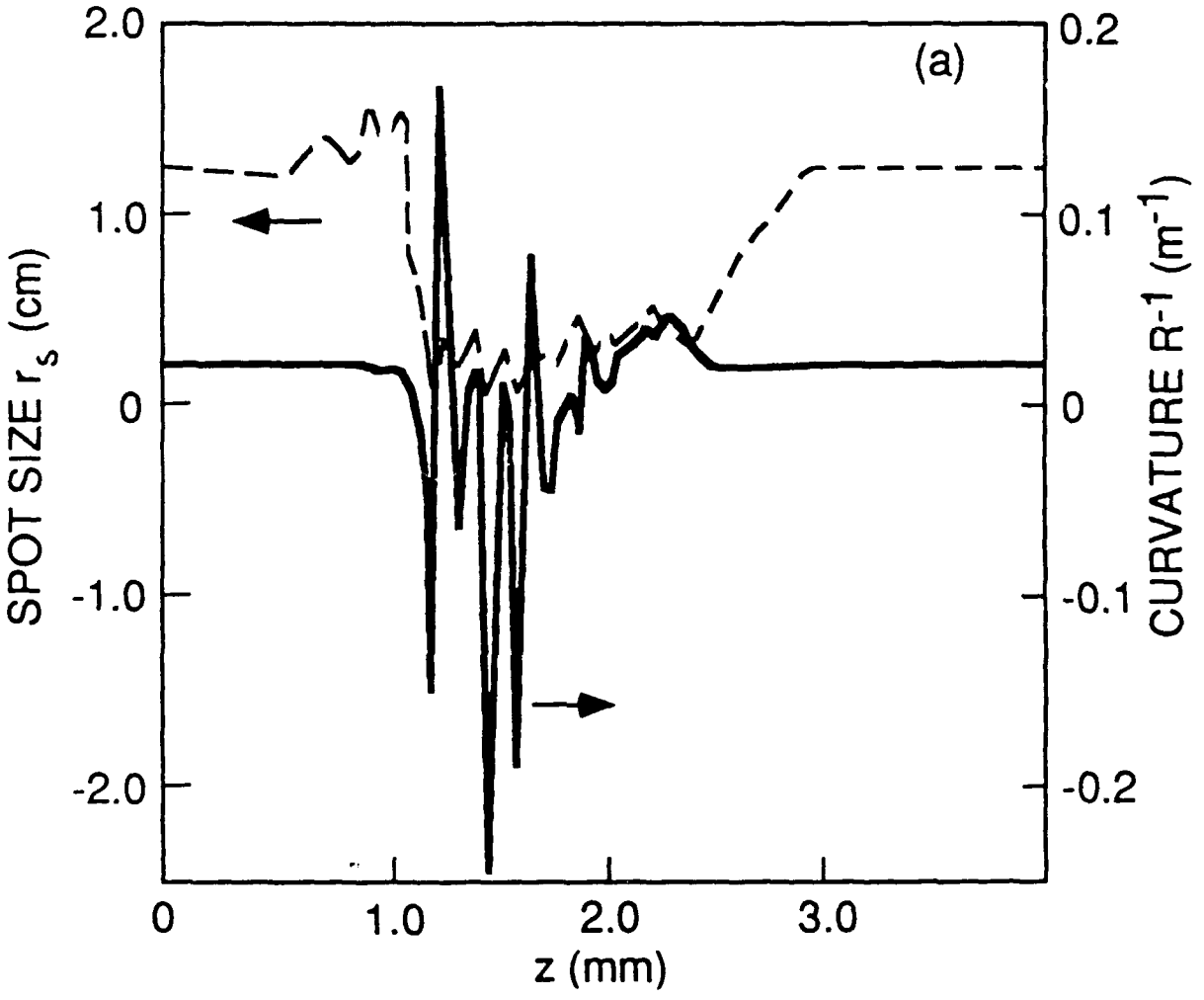

(a)

Fig. 9 Spot size $r_s(z)$ and curvature $R^{-1}(z)$ at wiggler exit. (a) slow taper, Case (a)

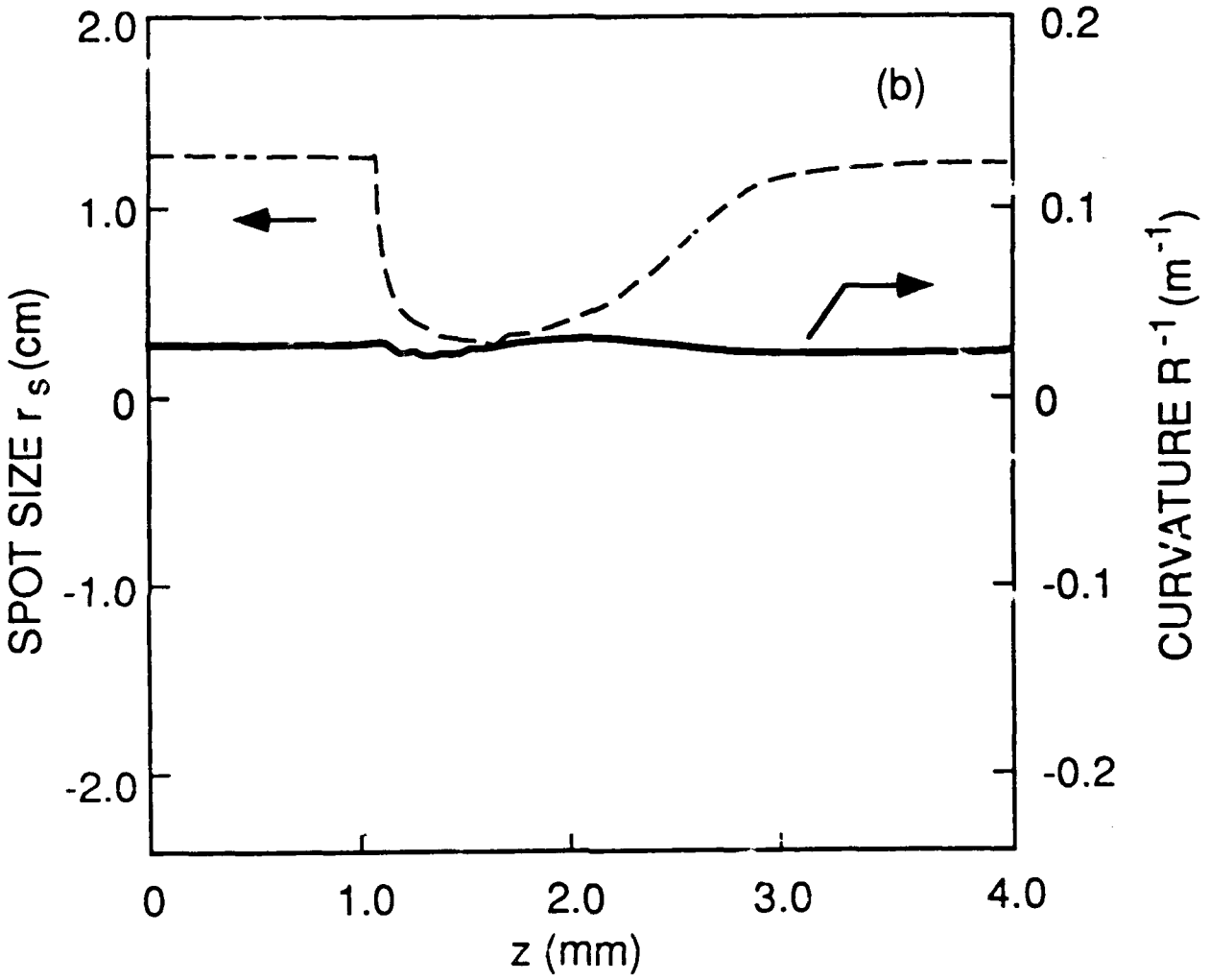

(b)

Fig. 9 Spot size $r_s(z)$ and curvature $R^{-1}(z)$ at wiggler exit. rapid taper, Case (b).

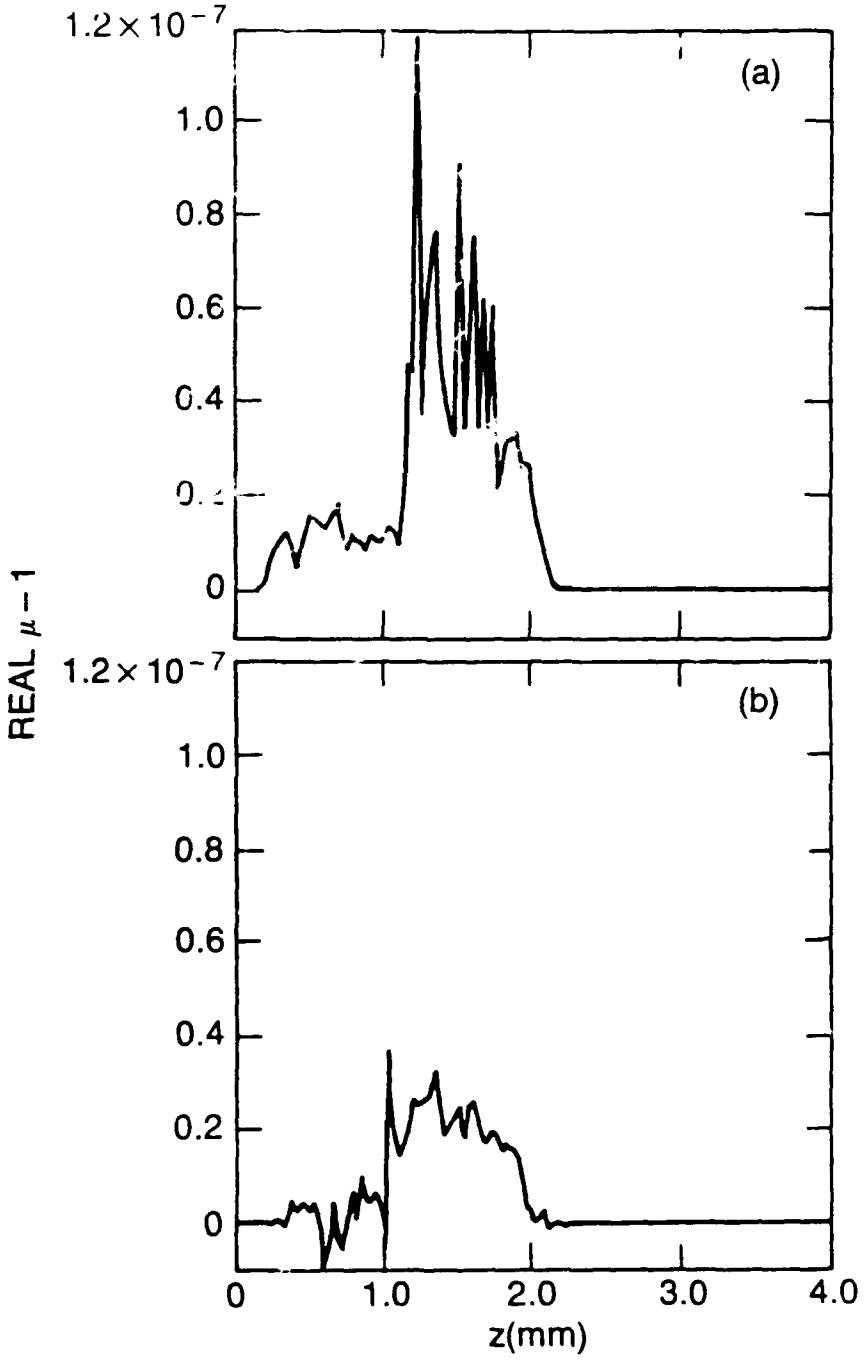

Fig. 10 Real μ(z,r=0) part of refractive index at wiggler exit. (a) slow taper, Case (a); (b) rapid taper, Case (b).

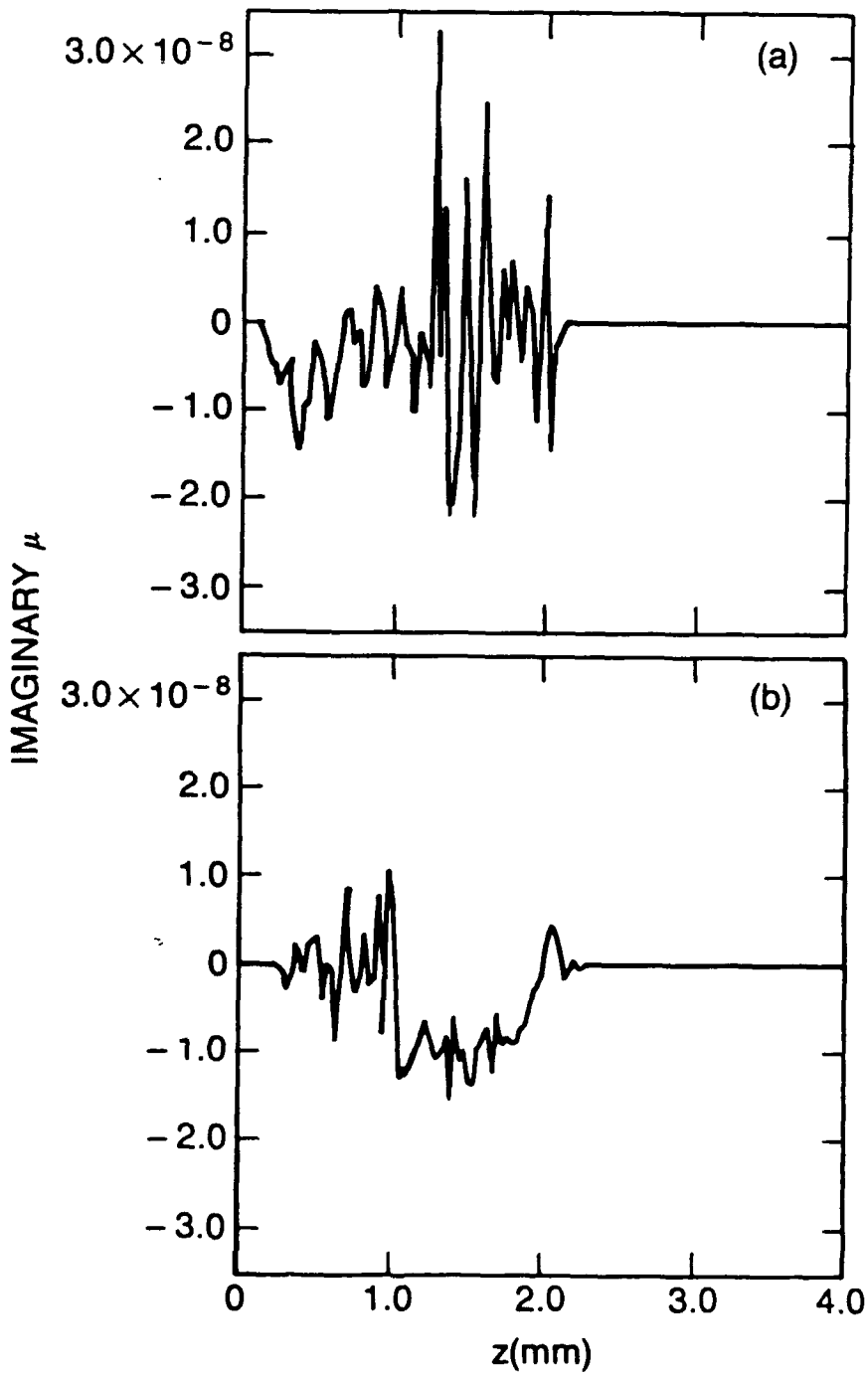

Fig. 11 Imaginary μ(z,r=0) part of refractive index at wiggler exit. (a) slow taper, Case (a); (b) rapid taper, Case (b).

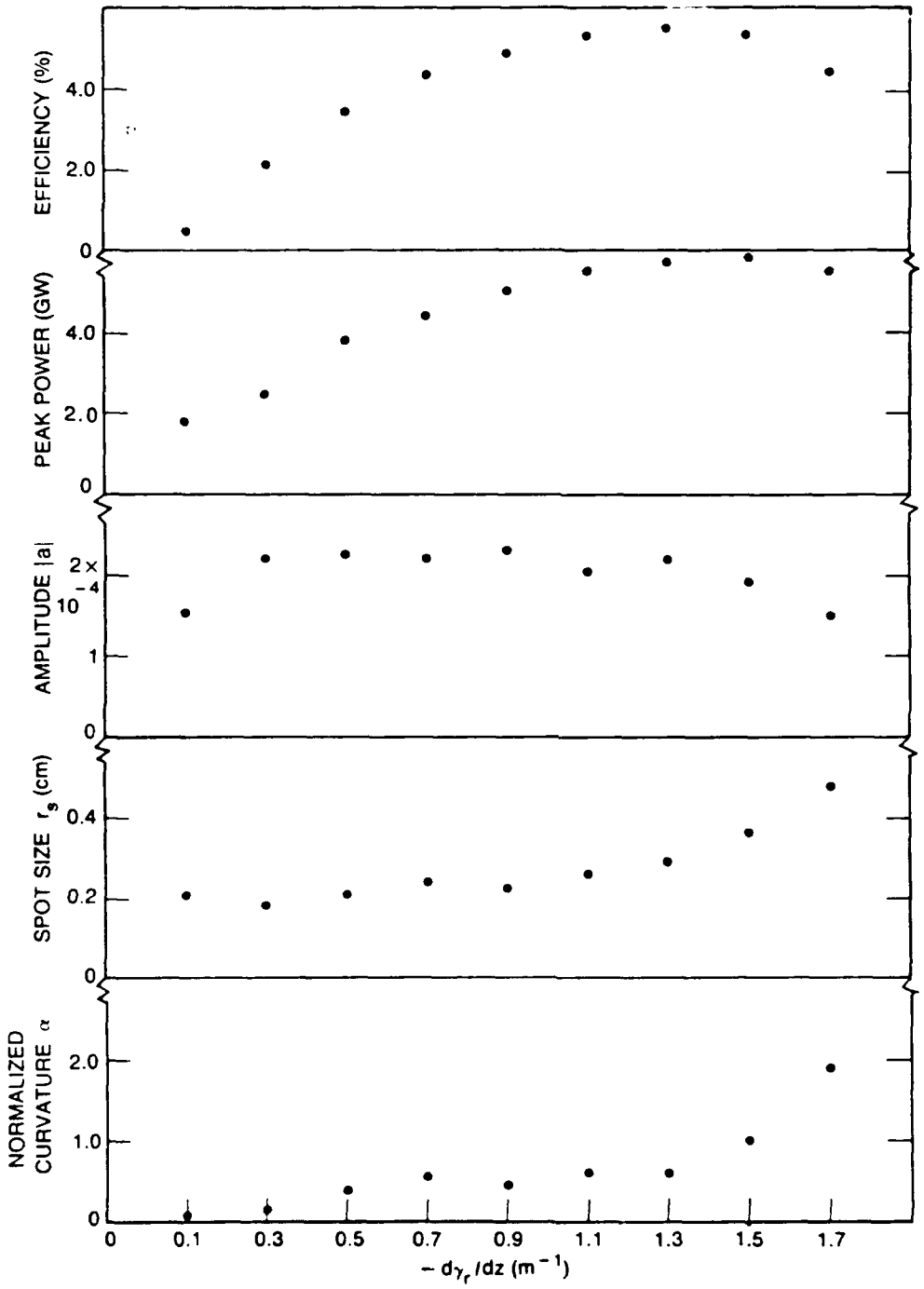

Fig. 12 Summary of results for various tapering rates $-d\gamma_r/dz$. Efficiencies are obtained from total energy in optical field. For other quantities, ordinate values correspond to peak-power point along the pulse, which varies somewhat between the different tapering rates.